Experimental and numerical study of the wake of a simplified automobile model with a variable rear slant angle

Claudia Vergueiro Massei
Instituto Tecnológico de Aeronáutica - ITA
claudia.massei@gmail.com

Valérie Ferrand
École Nationale Supérieure de l'Aéronautique et de l'Espace – Supaéro (Toulouse, France)

Paulo Afonso de Oliveira Soviero
Instituto Tecnológico de Aeronáutica - ITA
soviero@ita.br

Abstract. *This work studies the critical geometry case of the rear slant angle of a simplified car model together with the influence of the moving floor. Initially, the literature results concerning the drag of the critical geometry were experimentally validated. Next, the same experiments were carried out in the presence of a moving ground. To better understand the flow around the model and how the moving ground affects it, it was used the technique known as PIV – Particle Image Velocimetry. Last, the assembly was modeled on CFD software and the same tests were simulated, so that it would be possible to compare experimental and numerical results.*

1. Introduction

Among the objectives of subsonic aerodynamics research is the determination of overall pressure forces – mainly, lift and drag. For streamlined bodies, the major interest is generally in lift. On the other hand, in the bluff-body case there are always regions of separation generating pressure drag. In this situation, drag, rather than lift, is the major unknown and there is no general theoretical model to predict it, as there are the non-viscous flow models used for streamlined bodies. The existence of "critical geometries" is one of the reasons for systematic experiments. This concept is related to the drag exhibiting a local maximum with respect to some geometrical parameter of a body shape. Usually, the critical geometries are found by chance with no prior expectation of their behavior. As drag overshoots are often unsuspected and tend to involve complex types of flow, one has to rely on systematic experimental studies to identify critical geometries and analyze them. One case of critical geometry concerning road vehicles was reported by Janssen and Hucho (1974). Changing the angle of the rear slanted portion of the roof of a car, they observed that, for a small range of angles (25-35), overall drag exhibited a large overshoot. There was also an effect on the after body flow separation: the separation line was either at the top of the slanted surface, or at its bottom, depending on the angle. This case of critical geometry inspired this work. Nevertheless, when studying flows around vehicles in wind tunnels, it should be considered the use of a moving floor, in order to carry out the simulations in a more realistic way. Measurements show that floor movement reduces drag and lift and computational fluid dynamics can predict differences in the flow fields.

1.1. Literature review

There is a great dependence between the vehicle drag and its rear slant angle. Around 30°, drag increases considerably and is drastically reduced around 40°, remaining reasonably constant from there on. This observation has made car designers avoid the critical rear slant angles on their vehicles. As a result, passenger cars can be classified into three categories: squarebacks, fastbacks and notchbacks. It should be mentioned that the wake originated in each of the three cases has a different structure, which will be discussed further.
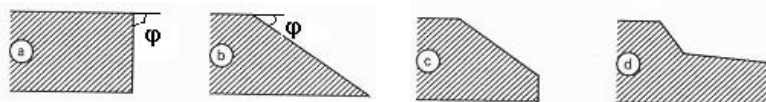

Figure 1. Different rear ends, schematic: squareback (a), fastback (b) (c), notchback (d).

The flow round a car body is characterized by separation and its drag is primarily pressure drag. There are typically two forms of separation at the rear end of vehicles: the quasi-two-dimensional, in the form of a wake, and the three-dimensional, as a longitudinal vortex pair. Frequently, both forms occur simultaneously; however, they are first discussed separately, on simplified models.

In Fig.(1), the primary rear end shapes are illustrated schematically. Shape (a), the full rear end ($\varphi > 30°$), most commonly called 'squareback', is typical for the quasi-two-dimensional separation bubble. This is because the boundary

layer cannot follow the steep pressure increase – at the rear edge – according to potential flow theory, and separates from the contour. This results in a considerably lower mean pressure coefficient Cp, than in friction-free flow, on the rear vehicle surface. A classical example for this is the airflow around a sphere: the difference of the pressures occurs only on the rear side of it and the pressure drag, therefore, is generated only there.

The three-dimensional separation with the formation of a pair of longitudinal vortices occurs on rear end shape (b) and (c), whose inclination are lower than the squareback one ($\varphi < 30°$). These kinds of shape are known as 'fastback'. A quasi-two-dimensional wake is also present at the perpendicular basis. Therefore, both types of separation can occur at the same time in this rear end shape.

The flow field for each of these configurations is illustrated in Fig.(2).
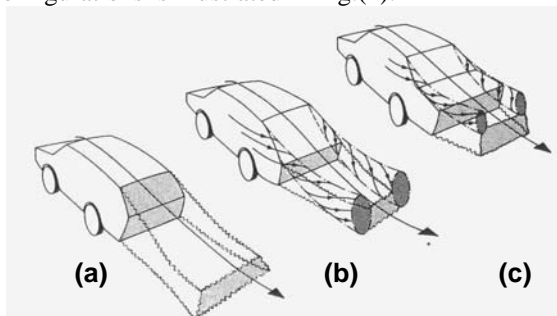

Figure 2. Flow pattern for different rear end configurations, schematic (Hucho, 1977).

In the light gray areas (a), the separation has a quasi-two-dimensional character. In this case, the line of separation tends to run perpendicular to the local flow direction. If reattachment occurs, separation bubbles are formed. The flow in these separation bubbles is unsteady, but there is a macrostructure with circulation in which the axes of the vortices run primarily perpendicular to the undisturbed flow, parallel to the line of separation. In some not very clarified way, the vortices of the separation bubble 'double back' in the shape of a horseshoe – see Fig.(4) – in the main flow direction at the side boundaries of the bubble and somehow they interfere with the exterior flow. The lower vortex rotates counterclockwise and the upper vortex, in the opposite sense. After the separation bubble closes, a pair of counter-rotating longitudinal vortices forms in the trailing wake. This produces an upwash in the case of a squareback, and induces a downwash in the trailing wake flow on a notchback or fastback.

Of course the flow inside the bubble, which is shed from a three-dimensional body, is three-dimensional in nature. However, since the separation itself is mainly two-dimensional, with the separation line normal to the flow and vortex axes parallel to separation line, it is designated 'quasi-two-dimensional'. This type of flow can occur at the leading edge of the front hood, at the sides on the fenders, on the cowl and on the front spoiler, and possibly in the notch of a notchback. Wakes are also formed on the blunt rear of a squareback. Depending on the outer flow field, long wakes are formed, which extend far downstream, or the wakes are short and closed – this will be explained right away.

The other type of separation, shown in Fig.(2) (b) and (c) by the dark gray areas, is three-dimensional in nature. A strong vortex pair – also known as C-pillar – is formed at the rear of the vehicle, depending on the inclination of the rear end. These rear vortices interact with the external flow field and with the quasi-two-dimensional wake and are similar to the tip vortices of a wing of low aspect ratio. They induce a downwash field in the space between their axes, which increases the tendency of reattachment in the central portion of the slanted surface and determines the position of the separation line for the wake. If the downwash is induced by a strong vortex pair, the separation line is quite low and a short wake is formed. If not, the flow separates at the upper edge of the roof and a long wake is formed. Last, it should be mentioned that this kind of separation isn't present in the squareback case.

The interaction between the C-pillar vortex pair ('tip vortices') and the vortex system of the quasi-two-dimensional separation bubble also depends on the rear slant angle.

With the squareback configuration, say 0° (or 90°), there are no 'tip vortices', but the stronger lower vortex in the wake, which rotates counterclockwise in the vicinity of the vehicle, generates an upwash with its developing horseshoe vortex, as explained above.

At a higher angle of inclination of the rear end, say 15°, the C-pillar vortex pair has developed. It induces a downwash, which forces the external flow downward in the area of the rear end and keeps it attached. This type of structure is responsible for a higher value of drag.

At 30°, the C-pillar vortices are highly pronounced, which induces very low pressure on the slanted part of the back and, consequently, increases drag considerably; the flow separates at the top or the bottom of the inclined rear end – depending upon the curvature of the rear edge of the roof.

At angles greater than 30°, the vortex burst increases the base pressure and the flow separates at the upper edge of the roof. C-pillar vortices are no more formed and a squareback flow regime is again present (with a limited recirculation zone), which makes the drag values become lower.

Between 10° and 15° the effect of the downwash-inducing C-pillar vortex pair and the upwash-inducing horseshoe vortex from the separation bubble counteract one another. The drag coefficient is at a minimum at these angles. However,

for 30° the C_D is at a maximum: the C-pillar vortices are so strong that flow remains attached over almost all of the sloping back, despite the large angle of inclination. This attached flow pattern is maintained by a supply of fluid from the sides of the body, which passes over the longitudinal vortices onto the slanted base, relieving the pressure rise along the central part of the inclined surface. Near the side edges of this surface, the wall pressure is expected to be much lower than in the center, due to the proximity of the rolled-up stream vortices – which usually have low pressure in their cores. The contribution to drag from these low-pressure regions is a manifestation of the energy continuously supplied into the edge-vortices. The evolution of the drag coefficient with the rear end slope angle is illustrated in Fig.(3) along with the schemas of separation line and wake for both fastback and squareback shapes.
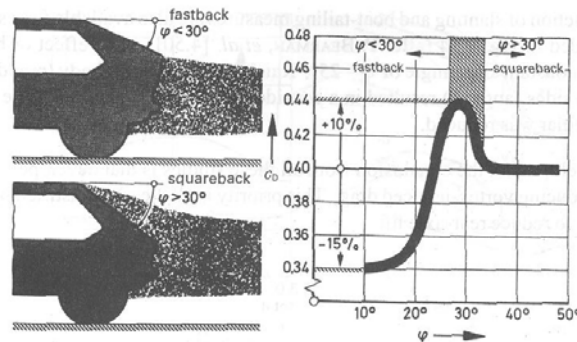

Figure 3. Influence of rear slant angle on drag, separation line and wake, measured on VW Golf (Janssen and Hucho, 1975)

The 'profile drag' of the three different rear end shapes is not equal because the position of the separation line changes when the flow pattern is changed from the fastback type into a squareback type and vice versa, i.e. the properties of the flow field around the 'profile' are significantly different. Therefore the profile drag will also change.

It is possible to summarize the vortex pattern for a sloping rear end as sketched in Fig.(4). In principle, there are three different vortex systems. Vortex C, emanating at the C-pillars, presents a 'potential flow' character. With the exception of a small viscous core area, its circumferential speed increases with decreasing radius (measured from the vortex centre). Its strength increases with the slant angle and, if the slant angle exceeds 30°, this vortex bursts and the flow pattern changes to the squareback flow regime. Vortex A and vortex B are the so called horseshoe vortices, generated in the quasi-two-dimensional manner at the edges A and B, respectively. They are of the viscous type and their vorticity is low. With inclined rearwards, as shown in Fig.(2), they are either dissipated or somehow merged into C-pillar vortices.
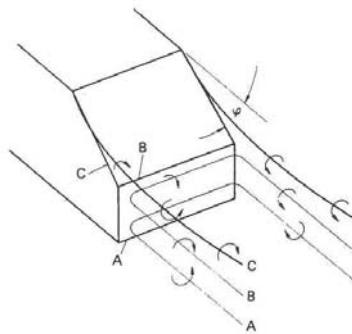

Figure 4. Vortex system for a sloping rear end, schematic (Hucho, 1977).

Finally, the flow along the underside of the vehicle is particularly unclear and suggests comparison with that on a very rough plate or with that in a narrow channel with one very rough wall.

Concerning the ground effect, the flow can be described by that around the body and its imaginary mirror image beneath the ground. As a result of the high speed, a force of attraction develops between the body and its mirror image – thus, a negative lift – which increases as the distance decreases. Circulation develops on the body due to friction effect, which results in a positive lift component. When considering three-dimensional flows, it should not be forgotten the lift induced by side and trailing vortices. This portion of the lift can be linked with the drag also induced by these vortices. As the vortices approach the ground they move slowly to the outside, as a result of the induction effect of their mirror image.

The experiments would be carried out with a simplified automobile model. The simplest model found in the literature consisted on an axisymmetric body (Bearmann (1979)). So, it was used a cylinder with a frontal disc as a model. The frontal disc played the role of assuring the reattachment of the flow at the beginning of the cylinder, avoiding, thus, a separation region over it. In the literature, there were only results available for the axisymmetric body off ground. This way, it is only possible to compare the off ground experiments results. The curve below (Fig.(5)) was extracted from Bearmann (1979) and, for this case, $Re = 10^6$.
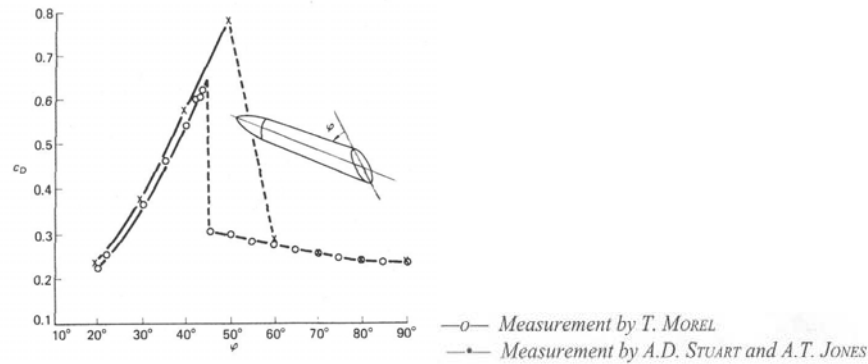
Figure 5. Effect of rear end slope angle φ on drag of an axisymmetric body off ground Bearmann (1979).

A study about the influence of a moving floor has been previously done by Bearmann, De Beer, Hamidy and Harvey (1988). Their conclusions were, basically, the following:

"The recirculation region is seen to be slightly longer above the moving floor and there are differences in flow direction beyond the region of reversed flow. Just downstream of the base and near the floor, the flow is seen to be nearly parallel with the moving floor, whereas the stationary floor data has a velocity component towards the floor. In this case, fluid appears to be being entrained into the boundary layer developing along the floor. Turbulence measurements indicate that the shear layer separating from the lower edge of the base spreads more rapidly in the stationary floor case and merges with the floor boundary layer."

However, "the flow immediately downstream of the base, within the wake, appears insensitive to floor movement."

2. Experimental methodology

The wind tunnel used in this work was equipped with a moving belt with a boundary layer suction system located upstream the belt, avoiding the problem of the wind tunnel inner boundary layer. To study the effects of this facility – especially its influence on the drag – all the experiments were carried out first with the belt off and, afterwards, with the belt on. In the latter case, the belt would always run at the same speed as the flow. The speed range of the experiments was from 10 m/s to 30 m/s, with the Reynolds number varying from $3.5 \ 10^4$ to $1.5 \ 10^5$.

It was used a cylinder linked to a frontal disc to simulate a simplified road vehicle. The position of this frontal disc also had an influence on drag. So, its distance was varied in order to find the optimal one – the one that would produce the minimum drag. The dimensions of the model (without its rear part) were as follows (Fig.(6)):
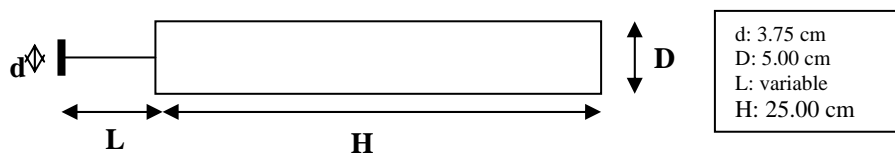

d: 3.75 cm
D: 5.00 cm
L: variable
H: 25.00 cm

Figure 6. Geometric configuration of the model.

The rear part of the model was removable, in order to test different rear slant angles (φ). There were 7 possible configurations: 0°, 10°, 20°, 30°, 40°, 50°, 90° (without the rear part).

The cylinder was sustained by a vertical mast connected to the balance above the tunnel. It must be mentioned that, before calculating the drag coefficient in every case, it would be necessary to suppress the drag value of the mast – obtained by testing only the mast, without the model – from the value of total drag obtained by the balance. By doing this, it would be possible to obtain the value of drag on the model only (without the influence of the mast). Figure (7) illustrates the wind tunnel (with the moving belt) and the model with one of its removable rear parts, by the time of the calibration of the balance.

The drag forces were measured by a balance with a pair of wire strain gages connected to a computer. By calibrating the balance, it was possible to find the relation between the forces applied to the model and the strain-gage signals produced by the change in their length. The range of calibration – from 0 to 200 grams – was estimated based on C_D values extracted from Bearmann (1979) for cylinders in the same conditions as ours and on known values of velocity, air density and reference area of the cylinder.
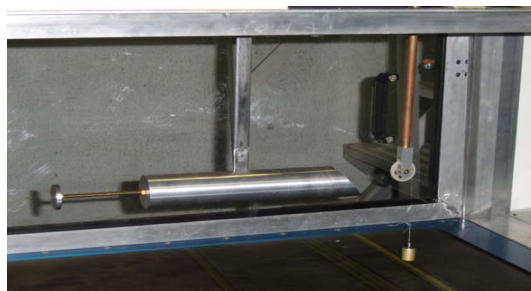
Figure 7. Assembly, with a rear slant angle of 50°, by the time of the calibration of the balance.

The Particle Image Velocimetry (PIV) is used to measure the velocity all over the flow field – even in the presence of high frequency oscillations of the fluid – without bringing a probe into it; thus, without disturbing the flow. Like the Laser Doppler Velocimetry, the Particle Image Velocimetry is based on the measurement of the velocity of tracer particles carried by the fluid. The advantage of the PIV-technique is that a complete section of the flow under investigation is illuminated, not only one single point of it. Images of the illuminated seeding particles are recorded, so that their displacement can be determined through the analysis of the records.

Initially, it was essential to define the type of seeding that would be used in the experiments: it was chosen to inject fluid-produced smoke into the wind tunnel. The illumination was provided by two pulsing laser beams located above the test section. First, PIV was carried out on the longitudinal plan; afterwards, on the transversal plan. To do that, it was necessary to turn the laser sheet and install a mirror inside the wind tunnel. The laser employed was the double-cavity Q-switched Nd: YAG type. The CCD camera was placed by the side of the wind tunnel, so that it would be perpendicular to the laser sheet. The camera faced the laser sheet directly in the case of the longitudinal plan. For the transversal plan, the mirror was placed at the end of the test section, at 45°, so that the camera would face the mirrored image directly and would record it. Next, it was necessary to regulate the focus of the camera – according to the position of the laser sheet, in order to properly see the particles in the illuminated section. After that, the scale factor was determined – the ratio between the real size of the object and the size of the image acquired by the camera. The necessary time between two pulses also had to be estimated in order to avoid loss-of-pairs in the longitudinal case. Since the scale factor was known, as well as the dimensions of the interrogation area in pixels, it was possible to calculate its dimensions regarding the wind tunnel. With this data and the wind velocity, the maximum time interval between two pulses necessary to photograph twice (on the two frames) the same particle in the same interrogation area could be estimated. For a better precision, this maximum time interval was used in the recordings. To avoid loss-of-pairs in the transversal case, it was necessary to work on the thickness of the laser sheet. A 3-milimeter sheet thickness was employed – a little bit more than twice the side of an interrogation area – to ensure that the particles wouldn't be able to completely cross the sheet in a 2-pulse time interval. A hundred images were recorded for each configuration tested, say 10°, 30° and 90° – with the moving belt both on and off – for both the longitudinal and transversal plans (the transversal plans were two: one at 1 cm from the cylinder and the other at 4 cm).

After recording the images, all of them were analyzed with the cross correlation method. This resulted in many instantaneous vector maps, which were validated with a peak validation process. With the validated maps, it was obtained an average vector field. This originated the vorticity fields together with the streamlines for all the maps. Only for the transversal tests, the velocity vertical component fields were obtained as well. For the longitudinal tests, the velocity maps inside the boundary layer were plotted – in order to specially compare the influence of the moving ground. It should also be mentioned that tests without the model were carried out in order to analyze only the test section with the PIV method.

3. Experimental results and analysis

3.1. Determination of the optimal distance disc-cylinder

"The position of the disc influences the intensity of the vortex wake. A turbulent boundary layer (in the absence of the disc, for example) generates a strong diffusion that makes the vortex sheet more spread and the vortices themselves less intense. This phenomenon affects drag directly, increasing it." (Morel, 1978).

By knowing that the position of the disc has an influence on drag, it would be interesting to find the optimal distance, this is, the distance that produces the minimum drag.

Figure (8) shows the behavior of the flow for different distances disc-cylinder. The first case, (a), illustrates the situation when the distance is less than the optimal one. The last one, (c), when the distance is greater than the optimal one. The other one, (b), is the optimal distance. This distance corresponds to the one for which the flow separates at the disc and reattaches right at the beginning of the cylinder, avoiding, thus, a separation region over the cylinder – as it is possible to observe in cases (a) and (c) – and a turbulent boundary layer, which would consequently increase drag, as explained above.
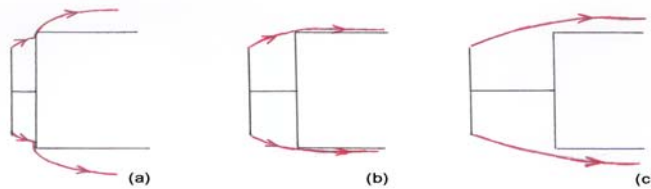
Figure 8. Possible distances disc-cylinder and flow behavior, schematic.

As a reference in the search of this optimal distance, it was used a previous study made by A. Roshko and K. Koenig in their book "Aerodynamic drag mechanism". Their purpose was to understand the behavior of the flow over two objects (cylinder and disc) placed one behind the other. They have observed that the interaction between the objects was positive and capable to lessen total drag. The minimum drag was achieved for the following geometry: d/D=0.75 and L/D=0.375. This information was withdrawn from the graph shown below in Fig.(9).
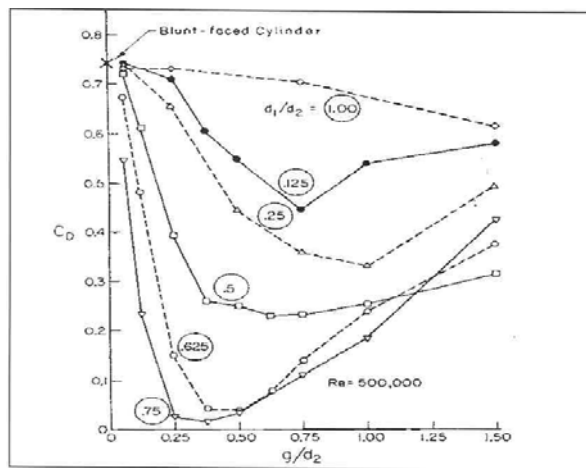

Figure 9. Drag coefficient evolution by A. Roshko and K. Koenig (Roshko and Koenig, 1974).

It must be noticed that the Reynolds number used to build this curve was 5.10^5, while the Reynolds in our case is around 5.10^4 or 7.10^4. Also, the cylinder of Roshko and Koenig wasn't placed near the ground as ours is. This implies one more reason to carry out this experiment and verify if the information found applies to this case.

So, with a disc to cylinder ratio d/D=0.75, drag was measured for different positions of the disc (L/D) and different velocities of the flow (10, 15, 20 and 30 m/s), either with and without the moving ground (moving at the same speed of the flow, for each case). The cluster was placed 5 mm from the ground and the rear slant angle of the cylinder was a right angle.

Since this study was a little bit more refined than that of Roshko and Koenig, 0.32 was found as the optimal L/D ratio for all the velocities tested – with and without the moving ground. One of the graphs obtained is plotted below on Fig.(10).
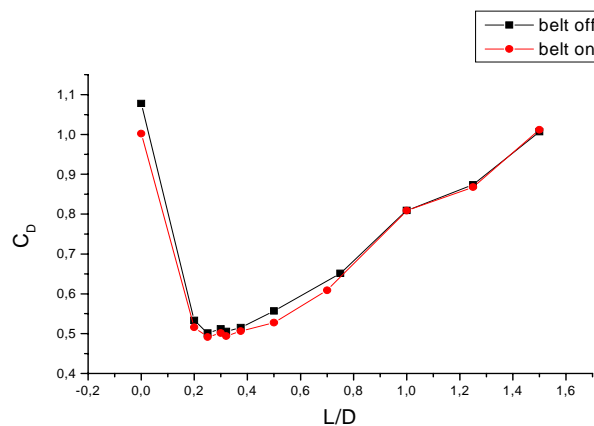

Figure 10. Determination of the optimal ratio L/D (flow velocity: 15 m/s).

Eventually, visualization tests with smoke were used to check and validate the optimal distance disc-cylinder found.

3.2. Influence of the rear slant angle and ground effect

With the ratio L/D = 0.32 fixed, the model was tested with the different rear parts to study the influence of the rear slant angle on drag. The cylinder was placed 5 mm from the ground and was tested at the same previous conditions (flow velocities of 10, 15, 20 and 30 m/s, both with and without the moving ground). Like this, it would be also possible to investigate the influence of the Reynolds number and the ground motion on the drag produced.

In order to analyze the influence of the ground on the previous experiments, the model was tested in the middle of the section – avoiding, thus, the ground effect – at those same velocities. The tests were made with the moving belt off to assure the symmetry of the section. These experimental results would be compared to the ones from Bearmann (1979).
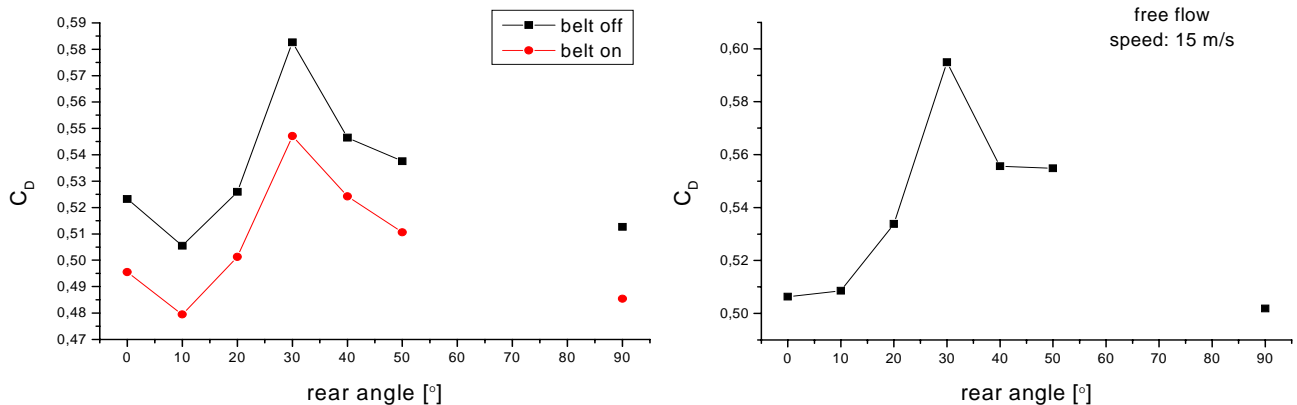

Figure 11. Influence of rear slant angle on drag near the ground and in free flow (Re: 5.5 10^4).

The curves present themselves according to the expected, based on theory. The 30-degree rear slant angle is the one responsible for the greatest value of drag coefficient, being, thus, its critical value. Also, C_D evolution follows two opposing trends that change at the critical value. In addition, it is remarkable that the 10-degree rear slant angle is the one that implies the least drag coefficient. Therefore, it can be evidenced a similar qualitative behavior between the curves that result from the measurements and the curves related to road vehicle tests found in the literature. Quantitatively, though, the C_D values found are higher than the literature ones. This might be due to the fact that a cylinder is less aerodynamic than a road vehicle and, being so, it is natural that its drag be higher. Furthermore, it is possible to notice that the C_D range of variation is practically the same, near 0.1, in both cases – measurements and literature.

Moreover, the C_D values for a 0-degree and a 90-degree rear slant angles are really close, which evidences that the cylinder's length doesn't influence its drag (the 90-degree rear slant angle corresponds to the cylinder without its rear part).

Evolution of the C_D values in free flow resembles, qualitatively, a lot that found in the literature (see Fig.(5)). The drag coefficients for 0-degree and 90-degree rear angles are basically the same; there is a monotonic crescent trend before the critical value; and, after the critical value, drag coefficient remains barely constant. Quantitatively, it is not possible to establish a comparison, once the shapes of the two bodies are different and the Reynolds numbers of the flows are completely different – the C_D values depend also on it.

3.3. Influence of the moving ground

The moving belt causes somewhat higher pressures near the front of the model. Because of the suppression of the lower boundary layer and the kinetic energy brought in by the moving belt, a larger volume of flow rate develops under the cylinder. Due to the continuity condition, a smaller volume of flow rate with higher pressures emerges above the cylinder, then. This change in the pressure distribution, according to further studies of Geropp and Odenthal (1996), affects drag directly, in a way that it always decreases when the ground is in motion.

3.4. Particle Image Velocimetry

3.4.1. Longitudinal tests

By analyzing the vector maps and, specially, the streamlines, it can be observed that the presence of the moving belt makes the fluid approach the ground. This is due to the fact that the lower boundary layer exists no longer (the velocity of the flow right above the belt is 15 m/s instead of 0 m/s), since the ground "pushes" the flow (this will be better exploited later) and makes it nearly parallel to the floor, "leaving room" for the fluid from above to come down. This makes the wake approach the ground as well. Sometimes the presence of the moving ground may influence as well the shape of the wake, "stretching" it - say, making it longer and less wide. This happens because the moving belt helps to develop the lower part of the wake – as can be seen for the case of the 0-degree slant angle cylinder.
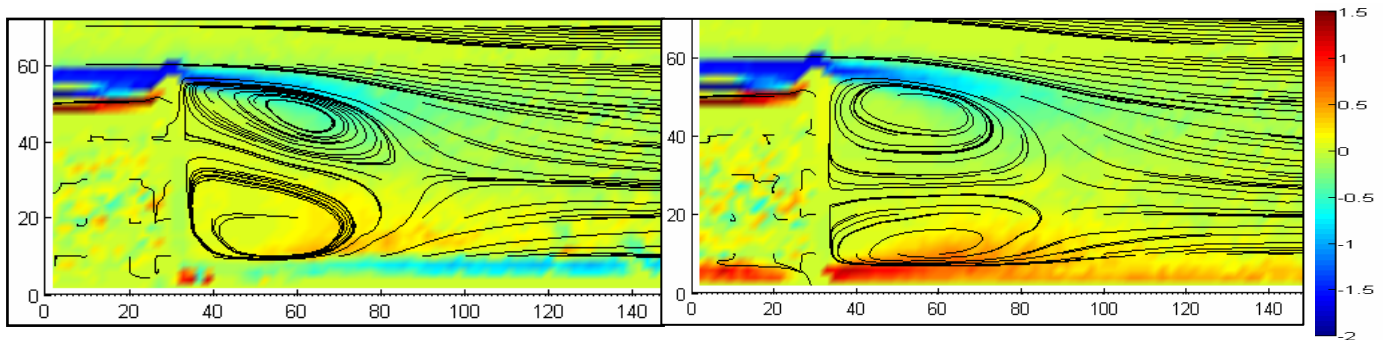
Figure 12. Streamlines and vorticity (10^4 s^{-1}) map for a 0-degree rear slant angle, belt off and on.

For the 0-degree slant angle cylinder, the flow separates completely at the end of the cylinder (as expected for a squareback car model) and the bubble closes practically at the same distance from the cylinder, not mattering whether the ground moves or not. Even though, the structures of both wakes are not the same. By analyzing the streamlines in Fig.(12), one can well remark that, with the belt on, the wake presents itself in a much more symmetric way.

In the case of the 10-degree slant angle, it is clear that the flow follows the rear slant, separating only at its end – just like for a fastback car model. It is also possible to identify that the recirculation bubble closes a little bit closer to the cylinder comparing to the 0-degree case.

In the case of the 30-degree slant angle, the flow remains attached to the rear slant until its end and there is an even smaller recirculation region. Figure (13) clarifies this difference.
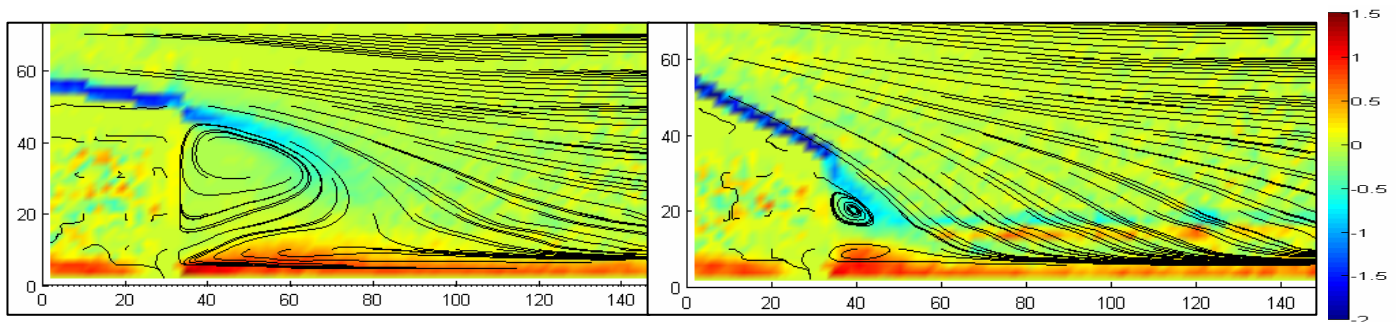

Figure 13. Streamlines and vorticity (10^4 s^{-1}) map for a 10 and a 30-degree rear slant angle, belt on.

It is also remarkable the upwash in the case of the right angle and the downwash in the 10-degree slant angle case, as previewed by theory (see "Introduction) for squarebacks and fastbacks, respectively. There is also a downwash in the case of the 30-degree slant angle. This fastback behavior makes sense once the flow has remained attached to the rear slant, just as it would remain on a fastback model.

Moreover, the vorticity maps show that the belt movement increases the vorticity of the flow near the ground – especially right after the cylinder, which is explained by the movement of the belt bringing vibration into the test section.
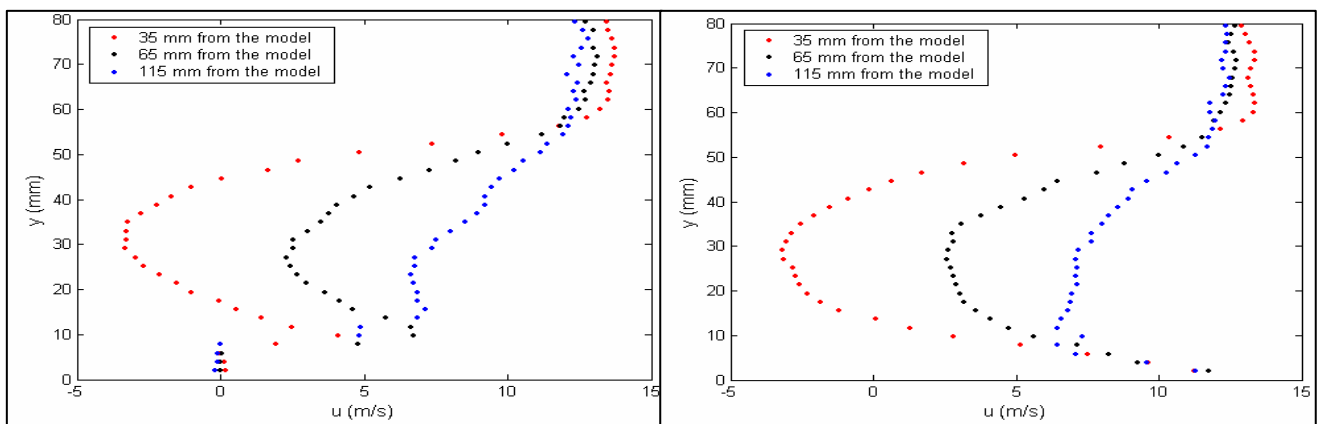

Figure 14. Velocity profiles for a 0-degree rear slant angle, belt off and on.
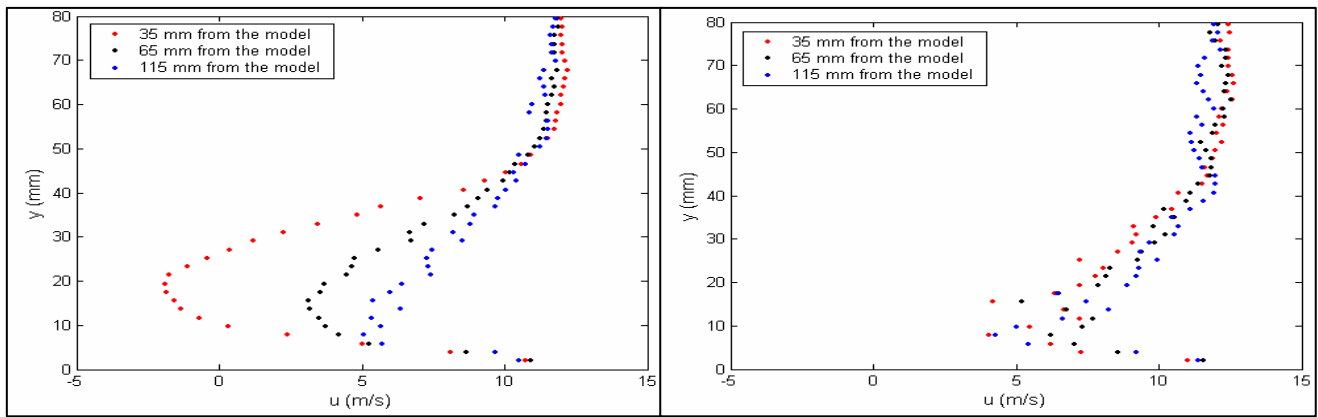
Figure 15. Velocity profiles for a 10-degree and a 30-degree rear slant angle, belt on.

The velocity profile maps evidence the fact already mentioned that the moving belt "pushes" the flow, once the velocity of the flow near the ground with the belt off is 0 m/s and with the belt on is near 12 m/s. The differences between the profiles at different distances from the model can also be remarked. The recirculation region impels to the fluid a lower (sometimes, even negative) velocity than the velocity of the flow. Since the recirculation bubble is larger closer to the cylinder, this effect is stronger the closer the point analyzed is to the model. This is also valid when comparing the profiles for different rear slant angles. For larger recirculation zones, lower velocities of the fluid are observed. This explains why the 0-degree slant angle model is the one that presents the lower velocity values. For values of height of 55 mm – the top of the cylinder – and greater, the velocity profiles present values of 12 m/s approximately constant. It is also possible to observe the velocity slightly greater as the point analyzed approaches the model and, consequently, the section entrance.

3.4.2. Transversal tests

First of all, it must be mentioned that the mirror placed in the section was responsible for deviating the flow; that is why the vector maps obtained presented the top vectors pointing to the left. This was also evidenced by the streamlines and the vector maps corresponding to the tests without the model. In the latter, it could also be verified that the deviation was not uniform in the section, which makes it even harder for its effects to be withdrawn.

By analyzing the vector maps, it has been possible to observe that, with the belt on, there was a greater vertical velocity component towards the floor at the bottom part of the field around the cylinder – in comparison with the belt off case. This could be justified by the fact – already explained – that the belt impels the longitudinal streamlines towards the ground, which decreases the fluid vertical velocity, making it more negative.
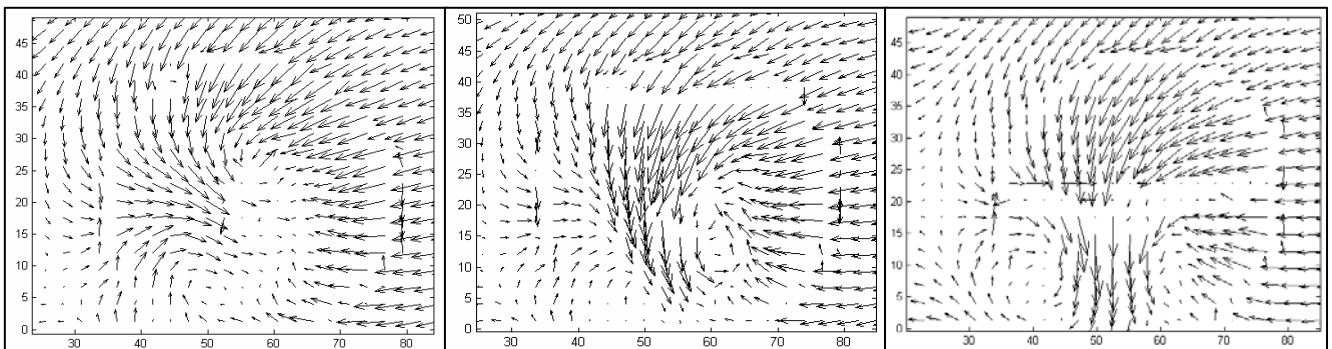

Figure 16. Vector maps for 0, 10 and 30-degree rear slant angles, belt on.

Figure (16) shows that, for the 0-degree slant angle cylinder, it is impossible to distinguish the vortex pair. It is only possible to see the movement of the particles that joined the recirculation bubble. In the case of the 10-degree one, it becomes possible to see the vectors at the bottom of the cylinder pointing towards the top and some vectors at mid-height pointing towards the center of the cylinder, indicating the vortex pair. Eventually, for the 30-degree case, one can already clearly visualize the vortex pair.

The vertical velocity maps were, then, analyzed in order to assure their symmetry. With the belt on, the vertical velocity all over the section was lower than it would be with the belt off. This was expected, just as explained above. For the 0-degree slant angle cylinder, the map was definitely not symmetric, which indicated the inexistence of a vortex pair. In the 10-degree case, it was possible to identify two symmetric steams that stood for high velocity values and indicated, approximately, the location of the vortex pair. Also for the 30-degree cylinder, but, in this case, the steams were larger.
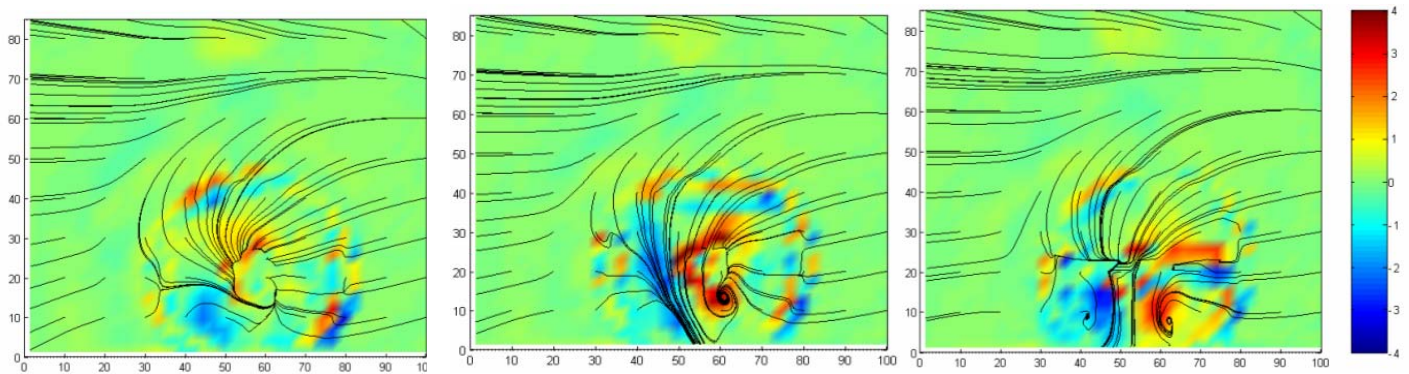
Figure 17. Streamlines and vorticity (10^3 s^{-1}) map 0, 10 and 30-degree slant angles, belt on.

The vorticity maps, illustrated in Fig.(17) led, basically, to the same conclusions as the vertical velocity ones. There was no vortex pair defined for the 0-degree rear angle cylinder. For the 10-degree one, there were, clearly, two steams – one blue and one red – that indicated the counter-rotating vortex pair. In the case of the 30-degree one, once again, the blue and red steams could be observed. This time, though, they presented themselves greater and more symmetric. The vortex pair was so intense that it could be distinguished from the streamlines as well.

This variation on the vortices intensity – already exploited in the introduction, explains the increase in drag when the rear slant angle is modified from 0 to 30 degrees. The more the vortices are pronounced, the lower the pressure they induce on the slanted part of the back – which contributes to a greater value of drag. For angles greater than 30 degrees, for example the right angle case, there are no longer vortices. This increases the base pressure and makes the flow separate, lowering drag at the same time.

The figures above result from tests at 4 cm from the cylinder. The same tests were carried out at the distance of 1 cm from the cylinder and the same effects, in less intensity, though, were observed. Even though the wake is larger closer to the cylinder, the structure of the vortex pair is not so well defined at this point. Concerning the analysis of the vector maps at 1 cm, for the 10-degree rear angle case, it was possible to see the vectors at mid-height of the cylinder pointing rearwards its center and some vectors near its edge pointing towards the top. This indicates that the vortex pair vertical position, at 1 cm from the model, is higher than the one at 4 cm from it; which shows that the vortices go down as they move away from the cylinder. As well, for the 30-degree slant angle cylinder, at 1 cm, it was possible to distinguish the vortex pair, vertically located a bit higher than in the 4 cm case. Coherently, on the vertical velocity maps, the vertical position of the steams that stood for high velocity values was higher than in the 4 cm case. In addition, the size of the steams was much smaller in the 1 cm case. This indicates that the vortices spring out as they move away from the cylinder – exactly as previewed in the theoretical part of this work. Concerning the vorticity maps at 1 cm, there were red and blue spots that fairly indicated the position of the counter-rotating vortex pair starting to develop. They were, again, smaller and vertically located a little bit higher than in the 4 cm case.

3.4.3. Tests without the model

The vector maps obtained evidenced that, with the belt on, there was a greater vertical velocity component towards the floor at the bottom part of the field. And, from the vorticity maps, one could tell that free flow had hardly any vorticity; this means that all the vorticity observed before was due to the presence of the model.

4. Computational Fluid Dynamics Method

Once having experimental results for three different rear slant angles, the next step would be obtaining the computational ones for the 30-degree rear slant angle cylinder. For such a task, it was necessary to build a mesh that would be solved later for the same boundary conditions as the ones from the experiments. The results obtained will be compared and commented in the next part of this work.

Producing a mesh starts by the conception of the virtual model geometry. This latter was done on the program CATIA. The geometry was, then, exported to the CFD program ICEM. Only after ensuring the good quality of the mesh, this one was exported to a solver; in this case, FLUENT.

4.1. CFD results and analysis

Regarding the longitudinal vector maps, the flow had a slight tendency of separating at the top of the rear slant base. On the other hand, it was remarkable that it remained attached to the base at its bottom. This instable behavior can be explained by the fact of dealing with a critical geometry – the 30-degree rear slant angle.

Just like observed experimentally, it was evidenced the downwash of the flow. Nevertheless, the recirculation region after the cylinder was not as evident as it was in the experimental maps.

Observing the velocity maps, it could be evidenced that the flow remained attached to the cylinder at its beginning, right after passing by the disc, just as it happened experimentally. It was also possible to compare the wakes obtained in each of the methods. Defining the wake as the region with velocity lower than 30% of free flow velocity, the wake obtained numerically was more stretched (narrower and longer) than the experimental one – which was more like an isosceles triangle. Nevertheless, their areas were pretty much the same.

Considering the vorticity maps, it was observed the same kind of difference there was between the belt on and belt off experimental cases. In the belt on case, there was more vorticity at the bottom base of the cylinder and in the region near the ground right after the cylinder than in the belt off case. In addition, the vorticity region after the cylinder follows the behavior of the wake, which is "stretched" by the action of the moving belt. So, this vorticity area after the cylinder is more "stretched" for the belt on configuration.

Concerning the effects of the moving floor, it can be stated that, without it, the flow under the cylinder presented two boundary layers: one attached to the cylinder and the other on the floor. Moreover, at the end of the cylinder, the flow below it presented almost zero velocity. However, when the belt was moving, the flow below the cylinder presented only one boundary layer – the one attached to it.
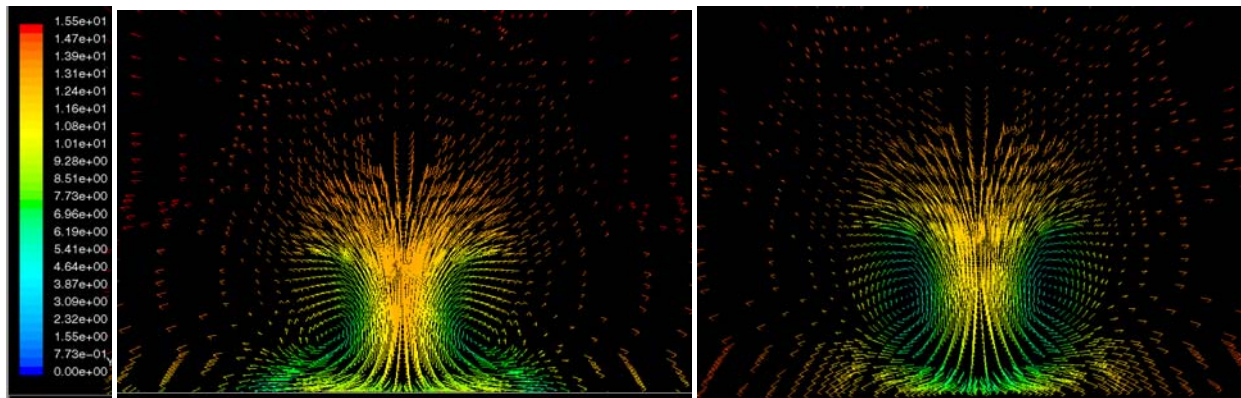

Figure 18. Vector map at 4 cm from the cylinder colored by velocity (m/s), belt off and on.

Concerning the transversal vector maps – shown in Fig.(18) and colored according to the total velocity magnitude – one could see that the counter-rotating vortices turned in the same sense as the experimental ones. In addition, it must be mentioned that, with the belt on, on a same given region of the section (except for below the cylinder), the velocity of the flow tends to be lower than it would be with the belt off. This can be explained by the continuity condition. With the belt on, there is more fluid that passes under the cylinder at a time. Consequently, there is less fluid that passes through the rest of the section, which makes a lower velocity all over this region. It could also be observed the fact that the vortices go down and spring out as they move away from the cylinder, as mentioned in the experimental results.

Regarding the vertical velocities maps, it was possible to evidence downwash from a region above the cylinder that presented negative vertical velocities. There were also two red steams and a blue central one, which showed the position of the vortices. Their analysis on both plans (1 cm and 4 cm from the cylinder) assures the fact that the vortices go down and spring out as they move away from the cylinder.

In the vorticity maps, Fluent gives only the vorticity amplitude, this is, only positive values. This way, it wasn't expected to have symmetric steams of different colors as there were in the experimental transversal vorticity maps, for example. It could be noticed, though, just like in the experimental results, that, for the 1 cm maps, the greater values of vorticity were concentrated at the edge of the cylinder; while for the 4 cm maps, they were concentrated at its center. Moreover, on the 1 cm maps, one could notice, again, that the action of the moving belt helped to increase vorticity near the ground right after the cylinder.
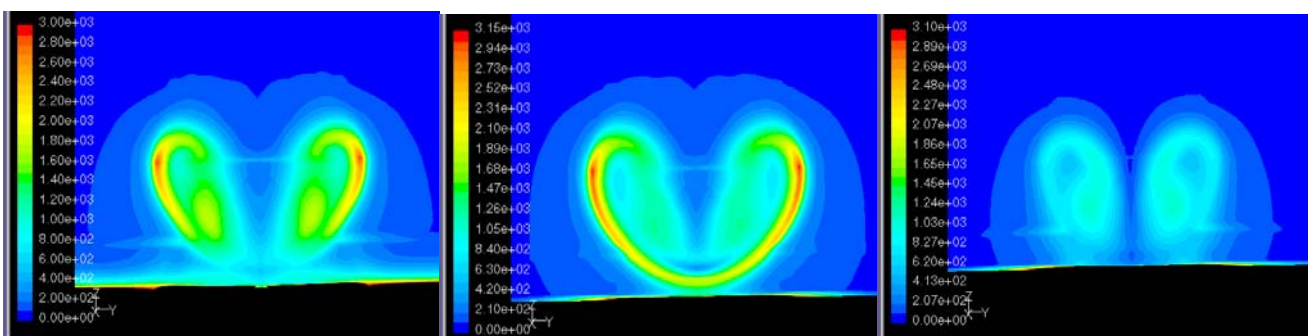

Figure 19. Vorticity (s^{-1}) map at 1 cm from the cylinder, belt off; belt on; and at 4 cm from the cylinder, belt on.

It must be mentioned that, although the qualitative behavior was likely for both experimental and numerical cases, the values of vorticity obtained numerically were not exactly compatible with the experimental ones. These latter are greater – even 3 times greater, especially for the longitudinal and the 4 cm cases. In fact, this might be due to experimental imperfections, such as irregularities on the belt surface that might bring in more vibration to the test section, image resolution problems in the PIV method, or even to the three-dimensionality of the flow, which might compromise the vorticity calculation, for example. At this point, the reader must be careful when considering the experimental results, since they don't agree with the numerical ones and it hasn't been possible to deeply investigate this issue.

5. Final remarks

It has been possible to evidence experimentally the results regarding the drag behavior when the rear slant angle of the model is modified. The obtained results were quite satisfactory and compatible with the existing literature data.

The Particle Image Velocimetry was useful to understand this behavior. The variation on the vortices intensity explains the increase in drag when modifying the rear slant angle from 0 to 30 degrees. The more the vortices are pronounced, the lower the pressure they induce on the slanted part of the back – which contributes to a greater value of drag. For angles greater than 30 degrees, for example the right angle case, there were no longer vortices. This increases the base pressure and makes the flow separate, lowering drag at the same time.

The CFD simulations were useful to compare the experimental data with the numerical one and to better analyze the influence of the moving ground. When comparing both methods, it is possible to notice that there are some "reality imperfections" – such as the mirror inside the wind tunnel, which generates a yawed flow, the real moving belt, the PIV system resolution – that keep one from obtaining the same data that could be obtained numerically. It is important to have these imperfections in mind not to absolutely thrust the experimental results. Regarding the influence of the moving ground, it could be evidenced a phenomenon described in the literature, but not experimentally measured. The reduction of drag by the movement of the belt is due to a change in the pressure distribution over the model. The action of the moving belt increases a lot the Cp values and also reduces, relatively, their range, making the pressure distribution more uniform. In addition, with the belt on, there were no longer negative values for Cp, as there were for the belt off case.

6. References

Bearmann, P.W., 1979, "Bluff body flows applicable to vehicle aerodynamics", Aerodynamics of Transportation, ASME-CSME-Conf. Niagara Falls, June 18th to 20th.

Bearmann, P.W., De Beer, D., Hamidy, E. and Harvey, J. K., 1988, "The effect of a moving floor on wind-tunnel simulation of road vehicles", SAE Technical Paper Series, International Congress and Exposition. Detroit, Michigan, February 29 – March 4.

Geropp, D. and Odenthal, H.J., 1996, "Drag reduction of motor vehicles by active flow control using the Coanda effect", Stanford.

Hucho, W.-H., 1977, "Aerodynamics of road vehicles from fluid mechanics to vehicle engineering".

Janssen, L.J. and Hucho, W.-H., 1975, "Aerodynamische Entwicklung von VW Golf und VW Scirocco", ATZ, Vol.77, pp 1-5.

Morel, T., 1978, "The effect of base slant on the flow pattern and drag of three-dimensional bodies with blunt ends", General Motors Research Laboratories, Warren, Michigan.

Roshko, A. and Koenig, K., 1974, "Aerodynamic drag mechanism".

7. Copyright notice